

Approximating Continuous Spectra of Hyperbolic Systems with Summation-by-Parts Finite Difference Operators

Brittany A. Erickson¹

¹Department of Computer Science, University of Oregon, Eugene Oregon, 97402, USA.

In this work we explore the fidelity of numerical approximations to continuous spectra of hyperbolic partial differential equation systems with variable coefficients. We are particularly interested in the ability of discrete methods to accurately discover sources of physical instabilities. By focusing on the perturbed equations that arise in linearized problems, we apply high-order accurate summation-by-parts finite difference operators, with weak enforcement of boundary conditions through the simultaneous-approximation-term technique, which leads to a provably stable numerical discretization with formal order of accuracy given by $p = 2, 3, 4$ and 5 . We derive analytic solutions using Laplace transform methods, which provide important ground truth for ensuring numerical convergence at the correct theoretical rate. We find that the continuous spectrum is better captured with mesh refinement, although dissipative strict stability (where the growth rate of the discrete problem is bounded above by the continuous) is not obtained. We also find that sole reliance on mesh refinement can be a problematic means for determining physical growth rates as some eigenvalues emerge (and persist with mesh refinement) based on spatial order of accuracy but are non-physical. We suggest that numerical methods be used to approximate discrete spectra when numerical stability is guaranteed and convergence of the discrete spectra is evident with both mesh refinement and increasing order of accuracy.

1 Introduction

Systems of hyperbolic partial differential equations emerge across vast application areas, from gravitational waves to drug delivery targeting cancerous tissues, to unsteady volcanic eruptions (1, 2, 3). Determining the physical growth and/or decay rates involved in such processes is the topic of many studies, for example (4, 5, 6, 7), as they reveal physical mechanisms for unstable phenomena. Such instabilities threaten, for example, the structural integrity of buildings and airplanes, and may indicate unstable dynamical growth that leads to regime changes in fluid systems.

When nonlinearities are present, the governing equations can be notoriously challenging to analyze and solve and are often linearized around a background and/or steady state solution. Even

so, analytic solutions can be difficult to obtain and one turns to numerical methods in order to explore the underlying physics and/or origin of unstable regimes. However, there are several stumbling blocks when using numerical methods to explore physical instabilities. Numerical methods, such as the finite difference method, can suffer from numerical instabilities, even when there are no physical instabilities present. And it is usually the case that numerical methods are used because analytic solutions are unavailable. If one observes an instability in the numerical simulation it is difficult to determine if it is numerical or physical in origin. These challenges persist when attempting to use discrete spectra to determine physical growth rates present in the model: the discretization can be incorrect (e.g. unstable) in the sense that numerical solutions will not converge to the analytic (and so the discrete spectrum will be incorrect even if it appears to converge). Alternatively, the discrete spectrum could appear to converge to eigenvalues that are artifacts of the numerical method but are non-physical.

In this work we explore the fidelity of numerical approximations to continuous spectra, focusing on variable-coefficient hyperbolic systems containing linear terms, which arise in perturbation studies (e.g. when nonlinear equations are linearized, for example in (3)). Using the Laplace transform, we derive the continuous spectra for several parameter regimes, as well as analytic solutions which provide ground truth for our numerical studies. We utilize a class of high-order-accurate finite difference methods satisfying a summation-by-parts (SBP) property (8, 9, 10). SBP methods together with a weak enforcement of boundary conditions through the simultaneous-approximation-term (SAT) technique provide a framework for provably stable numerical discretizations, see for example (11, 12, 13), which will provide the assurance that instabilities are not numerical in origin.

The paper is organized as follows. The governing equations considered are outlined in Section 2, with the continuous spectra derived in Section 3. Details of the SBP-SAT numerical discretization is given in Section 4, with numerical verification and derivation of analytic solutions in Section 5 and discrete spectra in Section 6. Conclusions follow in Section 7.

2 Governing Equations

We consider hyperbolic systems of the form

$$U_t + A(x)U_x = B(x)U + F(x, t), \quad x \in [0, L], \quad t \geq 0, \quad (1)$$

where F is a known source function, $A(x), B(x) \in \mathbb{R}^{2 \times 2}$ are spatially varying coefficient matrices where $A(x)$ is diagonalizable with real eigenvalues. We assume $A = V\Lambda V^{-1}$, with $\Lambda = \text{diag}(-\bar{c}(x), \bar{c}(x))$, which pertains to applications with information flowing in two directions at speed $\bar{c}(x)$, for example the Euler equations in fluid dynamics where $\bar{c}(x)$ is the fluid sound speed. $U = [u_1, u_2]$ is the vector of physical variables. For the 1D Euler equations, for example, $U = [v, \sigma]$, namely velocities and stresses. In most applications, boundary conditions are desired on the physical variables: for example consider the following Dirichlet and Neumann boundary conditions (respectively)

$$u_1(0, t) = g_0(t), \quad (2a)$$

$$\frac{\partial u_2}{\partial x}(L, t) = g_L(t), \quad (2b)$$

where g_0, g_L are the known boundary data. An energy estimate for (1) can be obtained through the diagonalization

$$W_t + \Lambda(x)W_x = \tilde{B}(x)W + \tilde{F}(x, t), \quad x \in [0, L], \quad t \geq 0, \quad (3)$$

where $\tilde{B} = -\Lambda V^{-1}V_x + V^{-1}BV$, $\tilde{F} = V^{-1}F$. We consider the general case where $\tilde{B}(x) = [a(x), b(x); c(x), d(x)] \in \mathbb{R}^{2 \times 2}$. Boundary conditions for (3) can therefore be written in general terms involving the characteristic variables $W = V^{-1}U$, namely

$$w_2(0, t) = R_0 w_1(0, t) + h_0(t), \quad (4a)$$

$$w_1(L, t) = R_L w_2(L, t) + h_L(t), \quad (4b)$$

where R_0, R_L are reflection coefficients. For example, non-reflecting/absorbing boundary conditions correspond to $R_0 = R_L = 0$. Dirichlet or Neumann conditions on physical variables are imposed by setting reflection coefficients to either 1 or -1, for example, boundary conditions (2) are imposed by setting $R_0 = 1, R_L = -1$ and taking $h_0(t) = 2g_0(t), h_L(t) = 2g_L(t)$. Other values for R_0, R_L correspond to Robin boundary conditions.

Supplementing (3)-(4) with the initial condition

$$W(x, 0) = f(x), \quad (5)$$

an energy estimate can be obtained by multiplying (3) by W^T , adding the transpose, and integrating by parts. This process yields the estimate

$$\begin{aligned} \dot{E} = & \bar{c}(L)(R_L^2 - 1)w_2^2(L) + \bar{c}(0)(R_0^2 - 1)w_1^2(0) + \\ & (W, \Lambda_x W) + (\Lambda_x W, W) + (W, \tilde{B}W) + (\tilde{B}W, W), \end{aligned} \quad (6)$$

where we define the energy $E = \|W\|^2$ using the L_2 scalar product and norm

$$(U, W) = \int_0^L U^T W dx, \quad \|U\| = \sqrt{(U, U)}. \quad (7)$$

Estimate (6) illustrates the well-known result that reflection coefficients should satisfy $-1 \leq R_0, R_L \leq 1$ for there to be no energy growth from the boundaries. Assuming this and letting $\alpha = \|\tilde{B}\| = \max_{\|U\|=1} \|\tilde{B}U\|$ and $\gamma = \|\Lambda_x\|$, applying the Cauchy-Schwarz inequality to (6) further reduces it to

$$\begin{aligned} \dot{E} & \leq (W, \Lambda_x W) + (\Lambda_x W, W) + (W, \tilde{B}W) + (\tilde{B}W, W) \\ & \leq (\gamma + \alpha)E. \end{aligned} \quad (8)$$

Equation (8) can be integrated in time to yield the final result

$$E(t) \leq \exp [2(\gamma + \alpha)t] E(0) = \exp [2(\gamma + \alpha)t] \|f\|^2, \quad (9)$$

which shows that energy in the system is bounded in terms of the data of the problem, i.e. the problem is well posed. Some exponential growth must be tolerated, however, due to the effects of \tilde{B} and Λ_x (the latter of which includes those from spatially varying wave speeds), see chapter 3 in (14).

3 Continuous Spectra

Specific rates of growth or decay associated with the initial boundary value problem (3)-(5) can be determined by computing the continuous spectrum. We denote the Laplace transform of a locally integrable function $h(t)$ by

$$\mathcal{L}[h] = \int_0^{\infty} h(t) \exp(-st) dt, \quad s \in \mathbb{C}. \quad (10)$$

Taking the boundary, source and initial data $h_0, h_L, F, f = 0$ and Laplace transforming in time yields

$$s\hat{W} + \Lambda(x)\hat{W}_x = \tilde{B}(x)\hat{W}, \quad x \in [0, L], \quad s \in \mathbb{C}, \quad (11)$$

where we use a hat to denote the Laplace transform. Equation (11) can be re-written as

$$\hat{W}_x = M(x, s)\hat{W}, \quad x \in [0, L], \quad s \in \mathbb{C}, \quad (12)$$

where

$$\begin{aligned} M(x, s) &= \Lambda^{-1}(x)(\tilde{B}(x) - sI) \\ &= \begin{pmatrix} -(a(x) - s)/\bar{c}(x) & -b(x)/\bar{c}(x) \\ c(x)/\bar{c}(x) & (d(x) - s)/\bar{c}(x) \end{pmatrix}. \end{aligned} \quad (13)$$

In this work we compute the associated analytic (i.e. continuous) spectrum, considering several cases for the spatially varying coefficients. Case 1 assumes constant coefficients and that \tilde{B} is a diagonal matrix. This is a particular case of the more general, but is useful for illustrative purposes. In Case 2 we still assume constant coefficients, but assume a slightly more general case where \tilde{B} is not diagonal. We then include some results for special cases of variable coefficients, namely Case 3 when \tilde{B} is still a diagonal matrix. We also include the set-up for Case 4 (the most general case) when \tilde{B} is not diagonal which will be explored in numerical studies. Note that for all of the cases we consider, the solution to (12) is given by

$$\hat{W}(x, s) = \exp\left(\int^x M(\xi, s)d\xi\right) C(s), \quad (14)$$

where $C(s) = [C_1(s), C_2(s)]$ are coefficients determined by the boundary conditions.

3.1 Case 1: Constant coefficients; \tilde{B} is a diagonal matrix

In this case we have that $b = c = 0$, thus the eigenvalues of M are given by

$$\lambda_{1,2}(s) = -(a - s)/\bar{c}, \quad (d - s)/\bar{c}, \quad (15)$$

with eigenvectors v_1, v_2 the standard basis vectors of \mathbb{R}^2 . Thus (14) reduces to

$$\hat{W}(x, s) = C_1(s) \exp[\lambda_1(s)x] v_1 + C_2(s) \exp[\lambda_2(s)x] v_2. \quad (16)$$

Substituting the Laplace transform of boundary conditions (4) into (16) yields the linear system $A(s)C(s) = 0$ where

$$A(s) = \begin{pmatrix} -R_0 & 1 \\ \exp[-(a-s)L/\bar{c}] & -R_L \exp[(d-s)L/\bar{c}] \end{pmatrix}. \quad (17)$$

As we are interested in non-trivial solutions to (12), we must have that $\det(A) = 0$, i.e.

$$R_0 R_L \exp[L\lambda_2(s)] - \exp[L\lambda_1(s)] = 0. \quad (18)$$

The above condition (18) is met at discrete $s_n \in \mathbb{C}$ which define the continuous spectrum, namely

$$s_n = \frac{(a+d)L + \bar{c} \ln(R_0 R_L) + 2\bar{c}\pi i n}{2L}, \quad n \in \mathbb{Z}. \quad (19)$$

Note that this result implies that the spectrum only exists if $R_0 R_L \neq 0$, namely, the two characteristic variables must be coupled at domain boundaries; a non-reflecting boundary condition will imply no continuous spectrum. Furthermore, values of s_n with positive real part can exist if either a or d (or both) are positive. For example, if $R_0 = R_L \in \{-1, 1\}$ (which is often the case as they correspond to Dirichlet/Neumann conditions), $\text{Re}(s_n) > 0$ if either a or d (or both) are positive, leading to physical growth of the system. On the other hand, Robin boundary conditions can counteract positive values of a and/or d , leading to energy decay.

3.2 Case 2: Constant coefficients; \tilde{B} is not diagonal

Here the eigenvalues of M are

$$\lambda_{1,2}(s) = \frac{-(a-d)}{2\bar{c}} \pm \frac{1}{2} \sqrt{\text{disc}(M)}, \quad (20)$$

where the discriminant of M is

$$\text{disc}(M) = \left(\frac{a-d}{\bar{c}} \right)^2 - 4 \left[\frac{bc - (a-s)(d-s)}{\bar{c}^2} \right]. \quad (21)$$

If $s \neq \frac{a+d}{2} \pm \sqrt{bc}$ (i.e. $\text{disc}(M) \neq 0$), then the eigenvalues of M are distinct, each with multiplicity 1. Since by assumption both b and c cannot both be zero, we assume WLOG that $b \neq 0$. Then the linearly independent eigenvectors of M corresponding to each eigenvalue are given by

$$v_{1,2} = [1, \quad [-(a-s) - \lambda_{1,2}\bar{c}]/b]. \quad (22)$$

In this case, $\det(A) = 0$ yields the equation

$$\begin{aligned} & \exp(\lambda_1 L) (-1 + R_L v_1^{(2)}) (-R_0 + v_2^{(2)}) + \\ & \exp(\lambda_2 L) (1 - R_L v_2^{(2)}) (-R_0 + v_1^{(2)}) = 0. \end{aligned} \quad (23)$$

Again, there is no spectrum if $R_0 R_L = 0$ (see Appendix A). If $R_0 = R_L = R \in \{-1, 1\}$ then (23) simplifies to

$$[\exp(\lambda_1 L) - \exp(\lambda_2 L)](-1 + Rv_1^{(2)})(-R + v_2^{(2)}) = 0. \quad (24)$$

We note that by inspection, the second two terms in (24) yield the real root

$$s_0 = \frac{a + R(b + c) + d}{2}. \quad (25)$$

Complex roots also exist when

$$\exp[\lambda_1(s)L] = \exp[\lambda_2(s)L], \quad (26)$$

(although by assumption, $\lambda_1 \neq \lambda_2$) and one can check that solutions to (26) are the roots

$$s_n^\pm = \frac{a + d}{2} \pm \sqrt{bc - \pi^2 n^2 \bar{c}^2 / L^2}, \quad n \in \mathbb{Z}^+ \setminus \{0\}, \quad (27)$$

which produces purely real roots for all $n \in \mathbb{Z}^+ \setminus \{0\}$ such that $bc \geq \pi^2 n^2 \bar{c}^2 / L^2$.

If $s = \frac{a+d}{2} \pm \sqrt{bc}$, then $\text{disc}(M) = 0$ and $\lambda = \frac{-(a-d)}{2\bar{c}}$ is the single eigenvalue of M , with multiplicity 2 and only one eigenvector. The general solution to (12) is thus

$$\begin{aligned} \hat{W}(x, s) = & C_1(s) \exp[\lambda(s)x] (I + x(M - \lambda(s)I))v_1 + \\ & C_2(s) \exp[\lambda(s)x] (I + x(M - \lambda(s)I))v_2, \end{aligned} \quad (28)$$

where v_1, v_2 are linearly independent solutions of $(M - \lambda I)^2 v = 0$, namely $v_1 = [1, 0]^T$ and $v_2 = [0, 1]^T$. Imposing boundary conditions (4) and seeking non-trivial solutions as before yields the equation

$$\begin{aligned} \exp[\lambda(s)L] \left[-R_0 \left(-\frac{bL}{\bar{c}} - R_L \left[1 + \frac{L}{\bar{c}} \left(\frac{a+d}{2} - s \right) \right] \right) - \right. \\ \left. \left(1 + \frac{L}{\bar{c}} \left[s - \frac{a+d}{2} \right] - R_L \frac{cL}{\bar{c}} \right) \right] = 0. \end{aligned} \quad (29a)$$

In the case that $R_0 = R_L = R \in \{-1, 1\}$, (29) reduces to

$$\exp[\lambda(s)L] \left[R \frac{L}{\bar{c}} (b + c) + \frac{L}{\bar{c}} (a + d - 2s) \right] = 0. \quad (30)$$

The second term in (30) yields the single real root s_0 .

For other values of R_0, R_L , roots of (23) are more challenging to compute analytically but could be determined numerically.

3.3 Case 3: Variable coefficients; \tilde{B} is a diagonal matrix

We first define the function

$$I_{\bar{c}/\delta}(x) = \int_0^x \frac{\delta(y)}{\bar{c}(y)} dy, \quad (31)$$

with $I_{\bar{c}}(x) = \int_0^x \frac{1}{\bar{c}(y)} dy$ corresponding to the time it takes to travel a distance x at speed $\bar{c}(x)$. We can write the general solution (14) as

$$\begin{aligned} \hat{W}(x, s) = & C_1(s) \exp \left[-I_{\bar{c}/a}(x) + sI_{\bar{c}}(x) \right] v_1 + \\ & C_2(s) \exp \left[I_{\bar{c}/d}(x) - sI_{\bar{c}}(x) \right] v_2. \end{aligned} \quad (32)$$

Application of boundary conditions and the desire for non-trivial solutions requires again solving $\det(A) = 0$, which yields the equation

$$R_0 R_L \exp \left[I_{\bar{c}/d}(L) - sI_{\bar{c}}(L) \right] - \exp \left[-I_{\bar{c}/a}(L) + sI_{\bar{c}}(L) \right] = 0, \quad (33)$$

which can be solved for the discrete eigenvalues

$$s_n = \frac{\ln(R_0 R_L) + I_{\bar{c}/d}(L) + I_{\bar{c}/a}(L) + 2\pi n i}{2I_{\bar{c}}(L)}, \quad n \in \mathbb{Z}, \quad (34)$$

which reduces to (19) in the case of constant coefficients.

3.4 Case 4: Variable coefficients; \tilde{B} is not a diagonal matrix

For this case it is quite difficult to compute an analytic spectrum since the matrix exponential in (14) can only be expressed as an infinite sum via the Magnus series (15). However, we include it here as we explore its spectrum numerically in Section 4.

4 SBP-SAT Finite Difference Approximation

Analytic solutions to the governing equations (3) - (5) can often be difficult to obtain and we turn to numerical methods. In this work we consider a class of high-order accurate finite difference methods known as summation-by-parts (SBP), with weak enforcement of boundary conditions through the simultaneous-approximation-term (SAT) technique. As opposed to traditional finite difference methods that “inject” boundary data by overwriting grid points with the given data, the SAT technique imposes boundary conditions weakly through penalization, so that all grid points approximate both the PDE and the boundary conditions up to a certain level of accuracy. The combined approach is known as SBP-SAT and provides a provably stable semi-discretization in space (11, 12, 16). The spatial derivative operators involve centered difference approximations within the domain interior, with a special transition to one-sided differences near domain boundaries. We use the diagonal norm SBP-SAT operators from (10) that have a formal order of accuracy given by $p = 2; 3; 4$ and 5 , with interior order of accuracy $2p + 2$ and boundary accuracy of $p + 1$.

4.1 Discrete Operators

The spatial domain $0 \leq x \leq L$ is discreteized with $N + 1$ evenly spaced grid points $x_i = 0 + ih, i = 0, \dots, N$ with grid spacing $h = 1/N$. A function u projected onto the computational grid is denoted by $\mathbf{u} = [u_0, u_1, \dots, u_N]^T$ and is often taken to be the interpolant of u at the grid points. The grid basis vector \vec{e}_j is defined to be a vector with value 1 at grid point j and 0 otherwise, which allows us to extract the j th component, namely $u_j = \vec{e}_j^T \vec{u}$.

We say that matrix \mathbf{D} is an SBP approximation to the first derivative operator $\partial/\partial x$ if it can be decomposed as $\mathbf{H}\mathbf{D} = \mathbf{Q}$ with \mathbf{H} being symmetric positive-definite and \mathbf{Q} satisfying $\vec{u}^T(\mathbf{Q} + \mathbf{Q}^T)\vec{v} = u_N v_N - u_0 v_0$. Here, \mathbf{D} is the standard central finite difference operator in the interior which transitions to one-sided at boundaries and \mathbf{H} is a diagonal, positive-definite matrix defining a discrete inner-product and norm, namely

$$(\mathbf{U}, \mathbf{W})_H = \mathbf{u}_1^T \mathbf{H} \mathbf{w}_1 + \mathbf{u}_2 \mathbf{H} \mathbf{w}_2, \quad \|\mathbf{U}\|_H^2 = (\mathbf{U}, \mathbf{U}), \quad (35)$$

where $\mathbf{U} = [\mathbf{u}_1^T \quad \mathbf{u}_2^T]^T$, $\mathbf{W} = [\mathbf{w}_1^T \quad \mathbf{w}_2^T]^T$.

4.2 Discretized Governing Equations

Equation (3) and boundary conditions (4) are discretized with the skew-symmetric SBP-SAT method (17, 18) as

$$\begin{aligned} \mathbf{W}_t + \Lambda_D \mathbf{W} = & \tilde{\mathbf{B}} \mathbf{W} + \alpha_0 \mathbf{H}_2^{-1} (\mathbf{w}_{2,0} - R_0 \mathbf{w}_{1,0} - h_0(t))(E_2 \otimes e_0) + \\ & \alpha_L \mathbf{H}_2^{-1} (\mathbf{w}_{1,N} - R_L \mathbf{w}_{2,N} - h_L(t))(E_1 \otimes e_N) + \tilde{\mathbf{F}}, \end{aligned} \quad (36)$$

where

$$\Lambda_D = 0.5(\Lambda \mathbf{D}_2 + \mathbf{D}_2 \Lambda) - 0.5 \mathbf{M}_{\bar{c}}, \quad (37)$$

for $\Lambda = \text{diag}(-\bar{c}, \bar{c})$ and $\mathbf{D}_2 = (\mathbf{I}_2 \otimes \mathbf{D})$. Here

$$\mathbf{M}_{\bar{c}} = \begin{pmatrix} -\text{diag}(\mathbf{D}\bar{c}) & \mathbf{0} \\ \mathbf{0} & \text{diag}(\mathbf{D}\bar{c}) \end{pmatrix}, \quad \tilde{\mathbf{B}} = \begin{pmatrix} \text{diag}(\mathbf{a}) & \text{diag}(\mathbf{b}) \\ \text{diag}(\mathbf{c}) & \text{diag}(\mathbf{d}) \end{pmatrix}, \quad (38)$$

which reduces to $\Lambda_D = (\Lambda \otimes \mathbf{D})$, $\tilde{\mathbf{B}} = (\tilde{\mathbf{B}} \otimes \mathbf{I})$ for constant coefficients. \mathbf{I} and \mathbf{I}_2 are the $N \times N$ and 2×2 identity operators, respectively, and we apply the Kronecker product to define $\mathbf{H}_2 = (\mathbf{I}_2 \otimes \mathbf{H})$. Here E_j is a 2×1 vector of zeros with a 1 in the j^{th} position and α_0, α_L are scalar penalty parameters. A discrete energy estimate determines values of the penalty parameters that yield a stable scheme, which may be obtained by taking $h_0 = h_L = \tilde{\mathbf{F}} = 0$ (not required but eases the computation). To aid the following analysis we rewrite (36) as

$$\mathbf{W}_t + \Lambda_D \mathbf{W} = \tilde{\mathbf{B}} \mathbf{W} + \mathbf{P} \mathbf{W}, \quad (39)$$

where

$$\begin{aligned} \mathbf{P} = & \alpha_0 \mathbf{H}_2^{-1} [(E_2 E_2^T \otimes e_0 e_0^T) - R_0 (E_2 E_1^T \otimes e_0 e_0^T)] + \\ & \alpha_L \mathbf{H}_2^{-1} [(E_1 E_1^T \otimes e_N e_N^T) - R_L (E_1 E_2^T \otimes e_N e_N^T)]. \end{aligned} \quad (40)$$

Multiplying (39) by $\mathbf{W}^T \mathbf{H}$ and adding the transpose yields the estimate

$$\begin{aligned} \dot{E}_h = & -\bar{c}_0 w_{1,0}^2 + \bar{c}_N w_{1,N}^2 + \bar{c}_0 w_{2,0}^2 - \bar{c}_N w_{2,N}^2 + (\mathbf{W}, \tilde{\mathbf{B}} \mathbf{W}) + (\tilde{\mathbf{B}} \mathbf{W}, \mathbf{W}) + \\ & (\mathbf{W}, \mathbf{M}_{\bar{c}} \mathbf{W}) + (\mathbf{M}_{\bar{c}} \mathbf{W}, \mathbf{W}) + (\mathbf{W}, \mathbf{P} \mathbf{W}) + (\mathbf{P} \mathbf{W}, \mathbf{W}) \\ = & -\bar{c}_0 w_{1,0}^2 + \bar{c}_N w_{1,N}^2 + \bar{c}_0 w_{2,0}^2 - \bar{c}_N w_{2,N}^2 + (\mathbf{W}, \tilde{\mathbf{B}} \mathbf{W}) + (\tilde{\mathbf{B}} \mathbf{W}, \mathbf{W}) + \\ & (\mathbf{W}, \mathbf{M}_{\bar{c}} \mathbf{W}) + (\mathbf{M}_{\bar{c}} \mathbf{W}, \mathbf{W}) + \\ & \alpha_1 w_{2,0} (w_{2,0} - R_0 w_{1,0}) + \alpha_2 w_{1,N} (w_{1,N} - R_L w_{2,N}), \end{aligned} \quad (41)$$

where $\mathbf{E}_h = \mathbf{W}^T \mathbf{H} \mathbf{W}$. Taking $\alpha_0 = -\bar{c}_0$, $\alpha_L = -\bar{c}_N$, estimate (41) reduces to

$$\begin{aligned} \dot{\mathbf{E}}_h &= -\bar{c}_0[w_{1,0}^2(1 - R_0^2) + (w_{2,0} - R_0 w_{1,0})^2] + \\ &\quad -\bar{c}_N[w_{2,N}^2(1 - R_N^2) + (w_{1,N} - R_N w_{2,N})^2] + \\ &\quad (\mathbf{W}, \tilde{\mathbf{B}}\mathbf{W}) + (\tilde{\mathbf{B}}\mathbf{W}, \mathbf{W}) + (\mathbf{W}, \mathbf{M}_{\bar{c}}\mathbf{W}) + (\mathbf{M}_{\bar{c}}\mathbf{W}, \mathbf{W}) \\ &\leq 2(\|\tilde{\mathbf{B}}\|_{\mathbf{H}} + \|\mathbf{M}_{\bar{c}}\|_{\mathbf{H}})\mathbf{E}_h, \end{aligned} \quad (42)$$

and thus a stable discretization, where the rate of change of the discrete energy mimics that of continuous case as in (6).

We note that the discrete energy estimate (42), places bounds on the solution at any final time T . This means that the numerical solution converges as the grid is refined but only on a compact domain in both space and time. Because we are interested in how a discretization approximates continuous growth/decay rates it is important to underscore that such stability estimates do not guarantee the the temporal evolution of the discrete system matches that of the of the continuous (which is ensured by a stronger notion known as strict stability, see (12)), which we will discuss in more detail in Section 6.

5 Analytic Solutions and Numerical Verification

To verify convergence of our numerical methods, analytic solutions are desirable. When $\tilde{\mathbf{B}}$ is a diagonal matrix and model data (e.g. \tilde{F} , h_0 etc.) are mostly zero, analytic solutions may be obtained via Laplace transform methods as in (19) without computations becoming too untractable. For more general cases of $\tilde{\mathbf{B}}$ and non-zero model data however, we may obtain analytic solutions using the method of manufactured solutions (20).

To illustrate the construction of an analytic solution via Laplace methods, we consider case 3 with $b(x) = c(x) = 0$, $h_0 = h_L = F = 0$, and initial data $f_1(x) = 0$, $f_2(x) \neq 0$. The solution to (3)-(5) is thus

$$\hat{\mathbf{W}} = \exp\left(\int_0^x \mathbf{M}(\xi, s) d\xi\right) \mathbf{C}(s) + \mathbf{G}(x, s), \quad (43)$$

where

$$\mathbf{G}(x, s) = [0, \quad G_2(x, s)]^T, \quad (44)$$

for

$$G_2(x, s) = \int_0^x \frac{f_2(\xi)}{\bar{c}(\xi)} \exp\left[I_{\bar{c}/d}(x) - I_{\bar{c}/d}(\xi) - s(I_{\bar{c}}(x) - I_{\bar{c}}(\xi))\right] d\xi, \quad (45)$$

or in component form

$$\hat{w}_1(x, s) = \exp\left[-I_{\bar{c}/a}(x) + sI_{\bar{c}}(x)\right] C_1(s), \quad (46a)$$

$$\hat{w}_1(x, s) = \exp\left[I_{\bar{c}/d}(x) - sI_{\bar{c}}(x)\right] C_2(s) + G_2(x, s). \quad (46b)$$

First we note that

$$G_2(x, s) = \exp\left[I_{\bar{c}/d}(x)\right] \mathcal{L}[f_2(\xi)H(\xi) \exp\left[-I_{\bar{c}/d}(\xi)\right]], \quad (47)$$

where H is the Heaviside function and xi is the characteristic variable defined implicitly by

$$t = I_{\bar{c}}(x) - I_{\bar{c}}(\xi). \quad (48)$$

We note that closed forms solutions therefore require that $I_{\bar{c}}(x)$ be invertible, which allows us to solve for ξ , namely

$$\xi(x, t) = I_{\bar{c}}^{-1}(I_{\bar{c}}(x) - t), \quad (49)$$

as in (19). Applying boundary conditions allows us to solve for the coefficients, namely, we have

$$C_1(s) = R_L R(s) G_2(L, s), \quad (50)$$

$$C_2(s) = R_0 R_L R(s) G_2(L, s), \quad (51)$$

where

$$R(s) = \frac{1}{\exp[-I_{\bar{c}/a}(L) + sI_{\bar{c}}(L)] - R_0 R_L \exp[I_{\bar{c}/d}(L) - sI_{\bar{c}}(L)]} \quad (52)$$

$$= \exp[I_{\bar{c}/a}(L) - sI_{\bar{c}}(L)] \cdot$$

$$\sum_{n=0}^{\infty} (R_0 R_L)^n \exp[n(I_{\bar{c}/d}(L) + I_{\bar{c}/a}(L) - 2sI_{\bar{c}}(L))], \quad (53)$$

where the geometric series in (52) converges for

$$\text{Re}(s) > \frac{\ln(R_0 R_L) + I_{\bar{c}/a}(L) + I_{\bar{c}/d}(L)}{2I_{\bar{c}}(L)}. \quad (54)$$

Thus we have solutions in Laplace space given by

$$\hat{w}_1(x, s) = \sum_{n=0}^{\infty} R_L (R_0 R_L)^n \exp[y_n(x) - s\alpha_n(x)] \mathcal{L}[f_2(\xi)H(\xi) \exp[-I_{\bar{c}/d}(\xi)]], \quad (55a)$$

$$\hat{w}_2(x, s) = G_2(x, s) + \sum_{n=0}^{\infty} (R_0 R_L)^{n+1} \exp[z_n(x) - s\beta_n(x)] \mathcal{L}[f_2(\xi)H(\xi) \exp[-I_{\bar{c}/d}(\xi)]], \quad (55b)$$

where

$$y_n(x) = (-I_{\bar{c}/a}(x) + I_{\bar{c}/a}(L) + n[I_{\bar{c}/d}(L) + I_{\bar{c}/a}(L)] + I_{\bar{c}/d}(L), \quad (56)$$

$$z_n(x) = (I_{\bar{c}/d}(x) + I_{\bar{c}/a}(L) + n[I_{\bar{c}/d}(L) + I_{\bar{c}/a}(L)] + I_{\bar{c}/d}(L), \quad (57)$$

$$\alpha_n(x) = -I_{\bar{c}}(x) + (2n + 1)I_{\bar{c}}(L), \quad (58)$$

$$\beta_n(x) = I_{\bar{c}}(x) + (2n + 1)I_{\bar{c}}(L) \quad (59)$$

which reduces to

$$y_n(x) = (-ax + aL + nL(a + d) + dL)/\bar{c}, \quad (60)$$

$$z_n(x) = (dx + aL + nL(a + d) + dL)/\bar{c}, \quad (61)$$

$$\alpha_n(x) = ((2n + 1)L - x)/\bar{c}, \quad (62)$$

$$\beta_n(x) = ((2n + 1)L + x)/\bar{c} \quad (63)$$

for constant coefficients. Applying the inverse Laplace transform to (46) then yields the following solutions

$$w_1(x, t) = \sum_{n=0}^{\infty} R_L (R_0 R_L)^n \cdot \exp \left[y_n(x) - I_{\bar{c}/d}(\xi_n) \right] f_2(\xi_n) H(\xi_n) H(t - \alpha_n(x)), \quad (64a)$$

$$w_2(x, t) = \exp \left[I_{\bar{c}/d}(x) \right] f_2(\xi) H(\xi) \exp \left[I_{\bar{c}/d}(\xi) \right] + \sum_{n=0}^{\infty} (R_0 R_L)^{n+1} \cdot \exp \left[z_n(x) - I_{\bar{c}/d}(\gamma_n) \right] f_2(\gamma_n) H(\gamma_n) H(t - \beta_n(x)), \quad (64b)$$

where

$$\xi_n(x, t) = \xi(L, t - \alpha_n(x)), \quad (65a)$$

$$\gamma_n(x, t) = \xi(L, t - \beta_n(x)), \quad (65b)$$

where $\xi(x, t)$ is defined by (49) and the argument (x, t) is dropped in (64) for notational ease. The solutions in (64) illustrate how $\bar{c}(x)$ determines the speed at which the initial data $f_2(x)$ is translated back and forth across the domain. Parameter $a(x)$ contributes to the spatial structure of the solution, whereas $d(x)$ (but not $a(x)$) contributes to exponential growth or decay in time, depending on its sign. However, if $f_1(x) \neq 0$ then a would also contribute to temporal exponential growth/decay.

For more complex solutions (for example where $h_0, h_L, F \neq 0$), one may manufacture an analytic solution. For example here we assume the analytic solution is (denoted with asterisks)

$$w_1^*(x, t) = \sin(\pi x - t) \quad (66a)$$

$$w_2^*(x, t) = \cos(2\pi x + t). \quad (66b)$$

Thus for any values of \bar{c} and matrix \tilde{B} , the corresponding source term is $\tilde{F}(x, t) = [\tilde{F}_1(x, t), \tilde{F}_2(x, t)]^T$ where

$$\tilde{F}_1(x, t) = - (1 + \bar{c}(x)\pi) \cos(\pi x - t) + a(x) \sin(\pi x - t) - b(x) \cos(2\pi x + t), \quad (67)$$

$$\tilde{F}_2(x, t) = - (1 + 2\bar{c}(x)\pi) \sin(2\pi x + t) + c(x) \sin(\pi x - t) - d(x) \cos(2\pi x + t), \quad (68)$$

and the boundary data is

$$h_0(t) = \cos(t) + R_0 \sin(t), \quad (69a)$$

$$h_L(t) = \sin(\pi L - t) - R_L \cos(2\pi L + t), \quad (69b)$$

Case	$a(x)$	$b(x)$	$c(x)$	$d(x)$	$\bar{c}(x)$
1a	-0.7	0	0	-1.3	1.2
1b	0.7	0	0	1.3	1.2
2a	1	-3	3	-5	1.2
2b	2	3	2	4	1.2
3a	$-0.7 - x$	0	0	$-1.3 + 0.1x$	$1.2 + 0.5x$
3b	$0.7 + x$	0	0	$1.3 + 0.1x$	$1.2 + 0.5x$
4a	x	$-3x$	$3x$	$-5x$	$1.2 + 0.5x$
4b	$2 + x$	$3x$	$2x$	$-1 + 4x$	$1.2 + 0.5x$

Table 1: Values for the variable coefficients for Cases 1-4.

for any length L and reflection coefficients.

For the numerical verification we take $R_0 = R_L = 1$, $L = 2$ and consider 2 variants of all 4 cases, listed in Table 1. Note that we limit our investigation of variable coefficients to smooth, linear functions; the effects of nonlinear and/or non-smooth coefficients can be found in (21, 19). For Cases 1 and 3 we verify with the analytic solution (64) using $f_2(x) = \exp[-(x - L/2)^2/\sigma^2]$ with $\sigma = 0.2$. The temporal evolution of the analytic and numerical solutions for case 1b (where physical growth is present) is illustrated in Figure 7. For Cases 2 and 4 we use the manufactured solution (66). Initial conditions, boundary and source terms are set by the exact solutions and we simulate over the temporal interval $0 \leq T$. For case 1 we set $T = 3$ and for cases 2-4 we take $T = 0.1$.

We denote the total error in the discrete \mathbf{H} -norm by

$$E(t) = \|W^*(\cdot, t) - \mathbf{W}(\cdot, t)\|_{\mathbf{H}}, \quad (70)$$

where $W^* = [w_1^{*,T} \quad w_2^{*,T}]^T$ is the stacked analytic solution vector. At the final time with compute the relative error

$$\tilde{E} = \frac{\|\mathbf{W}(T) - W^*(\cdot, T)\|_{\mathbf{H}}}{\|W^*(\cdot, T)\|_{\mathbf{H}}}, \quad (71)$$

where $W^*(\cdot, T)$ is the analytic vector solution evaluated on the grid. Time stepping is done via an adaptive Runge-Kutta scheme with time step sufficiently small so that error is confined to that in space. Figures 1-4 illustrate convergence for all cases at the theoretical rate.

6 Discrete Spectra Approximations

Applying the Laplace transform to discretization (39) yields the eigenvalue problem

$$s\mathbf{W} = \mathcal{D}_h\mathbf{W}, \quad (72)$$

where $\mathcal{D}_h = (-\Lambda_D + \tilde{\mathbf{B}} + \mathbf{P})$, whose eigenvalues correspond to the discrete spectrum. For Cases 1-4 we explore how well this discrete spectrum approximates the continuous. Ideally the discrete spectra does not overly predict the rate of temporal evolution in the physical problem, which would be the case if the discrete spectra converge to the continuous from the left, a feature that indicates strict stability of dissipative type of the numerical scheme (21, 19). This is important for long-time

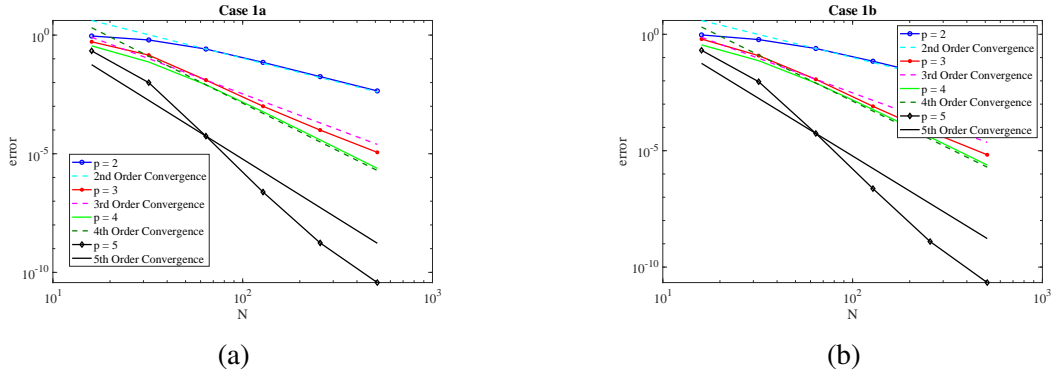


Figure 1: Convergence rates for SBP operators with order of accuracy $p = 2; 3; 4; 5$ for (a) case 1a and (b) case 1b. Relative error computed at $T = 3$, with convergence achieved at the expected rates.

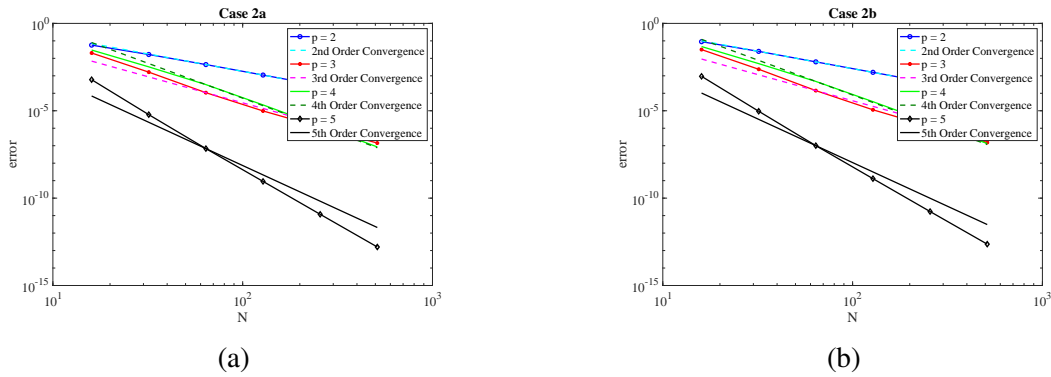


Figure 2: Convergence rates for SBP operators with order of accuracy $p = 2; 3; 4; 5$ for (a) case 2a and (b) case 2b. Relative error computed at $T = 0.1$, with convergence achieved at the expected rates.

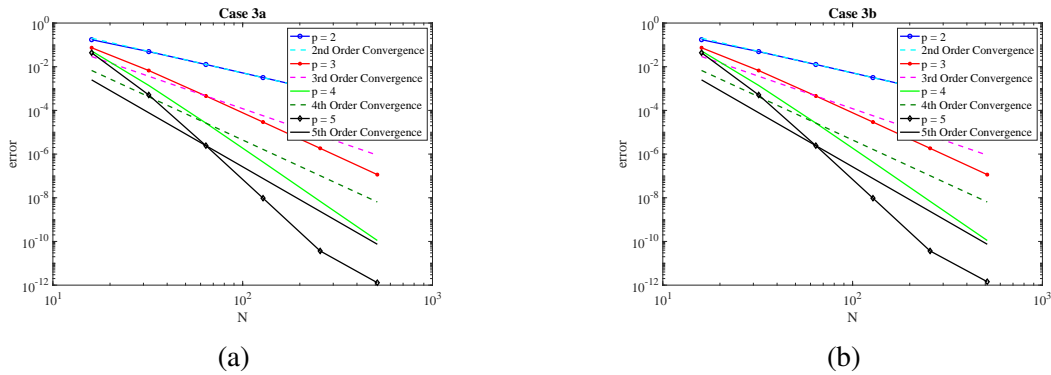


Figure 3: Convergence rates for SBP operators with order of accuracy $p = 2; 3; 4; 5$ for (a) case 3a and (b) case 3b. Relative error computed at $T = 0.1$, with convergence achieved at the expected rates.

calculations so that high-frequency errors do not grow and destroy the accuracy. However we are primarily interested in determining when discrete spectra correctly identify positive modes of

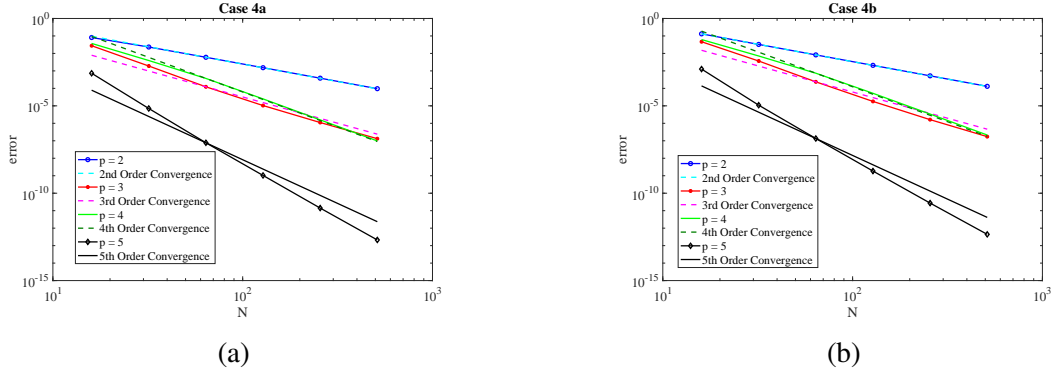


Figure 4: Convergence rates for SBP operators with order of accuracy $p = 2; 3; 4; 5$ for (a) case 4a and (b) case 4b. Relative error computed at $T = 0.1$, with convergence achieved at the expected rates.

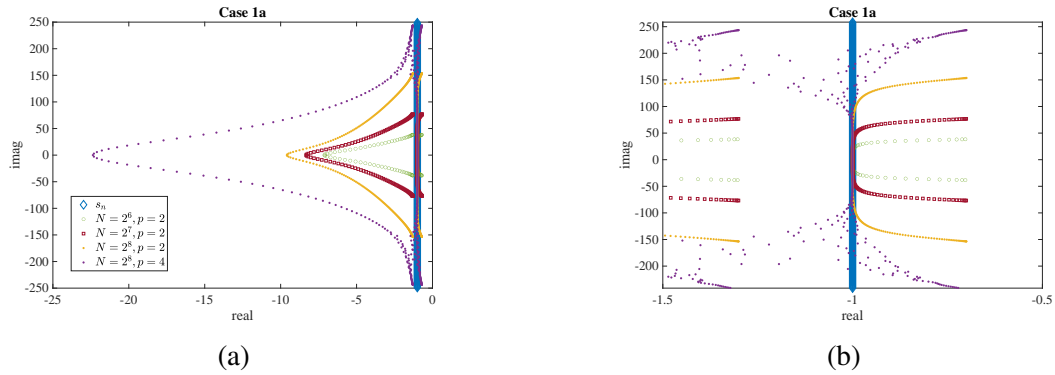


Figure 5: (a) Analytic and numerical spectrum for Case 1a, where $a = -0.7, b = c = 0, d = -1.3$ with (b) zoom.

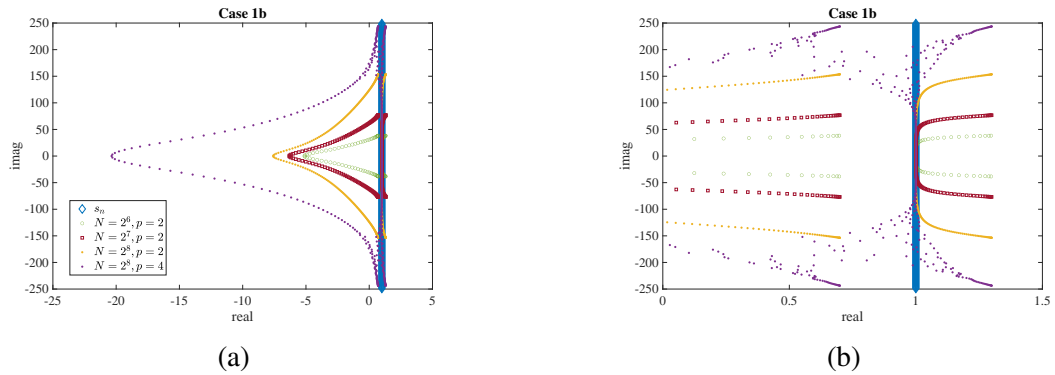


Figure 6: (a) Analytic and numerical spectrum for case 1b, where $a = 0.7, b = c = 0, d = 1.3$ with (b) zoom.

growth.

For Case 1a the analytic spectrum is $s_n = -1 + 0.6\pi in$, $n \in \mathbb{Z}$. In Figure 5 we plot this along with the discrete spectrum for increasing number of grid points N , with $p = 2$ and also for one

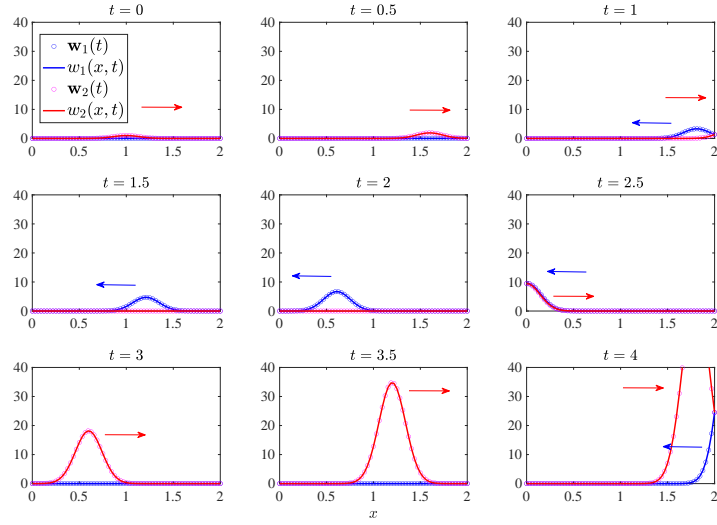


Figure 7: Temporal evolution of the analytic and numerical approximation to the solution corresponding to Case 1b using $p = 2$, $N = 2^{10}$, where exponential growth is present in the physical problem. Initial condition is a Gaussian pulse on w_2 (red), centered at zero, which initially propagates to the right (direction of pulse propagation denoted with arrows and colors correspond to the solution component), is reflected to w_1 (blue) which then propagates to the left etc. Time denoted above subfigures.

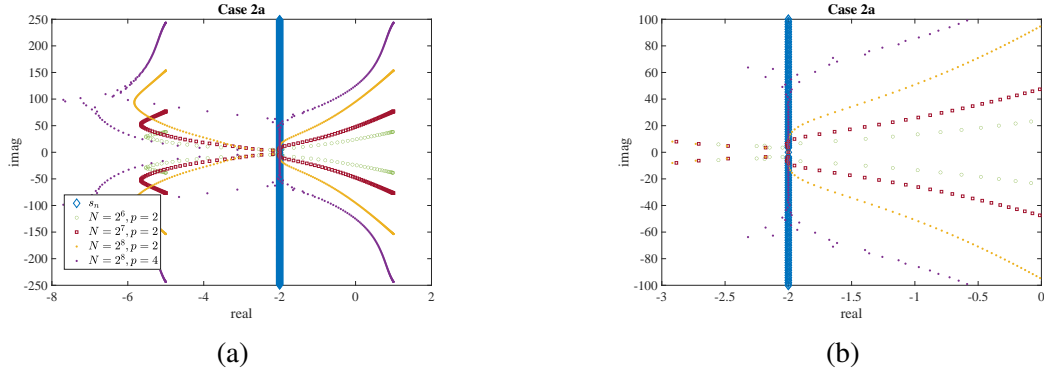


Figure 8: (a) Analytic and numerical spectrum for case 2a, where $a = 1$, $b = -3$, $c = 3$, $d = -5$ with (b) zoom.

case of $p = 4$. The physical problem dictates exponential decay since $\text{Re}(s_n) < 0$, and the left figure shows that the discrete spectra lies entirely in the left half of the complex plane. However, the zoom on the right reveals that some of the discrete eigenvalues lay to the right of s_n , indicating that dissipative strict stability is not obtained, a feature that persists for all the cases we consider in this work. However, as the mesh is refined or if p is increased, more discrete eigenvalues align with s_n , indicating convergence of the discrete spectrum. We also observe that the real part of the discrete spectrum is bounded above by $a = -0.7$. For Case 1b, the analytic spectrum is given by

$$s_n = 1 + 0.6\pi in, \quad n \in \mathbb{Z}, \quad (73)$$

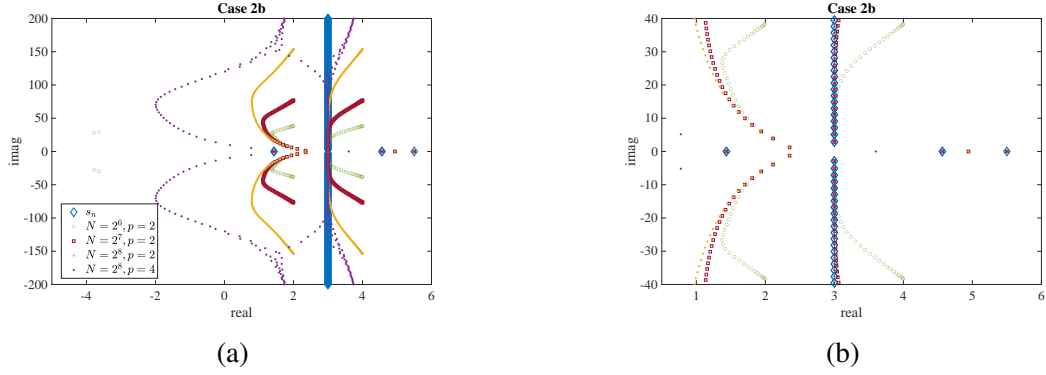


Figure 9: (a) Analytic and numerical spectrum for case 2b, where $a = 2, b = 3, c = 2, d = 4$ with (b) zoom.

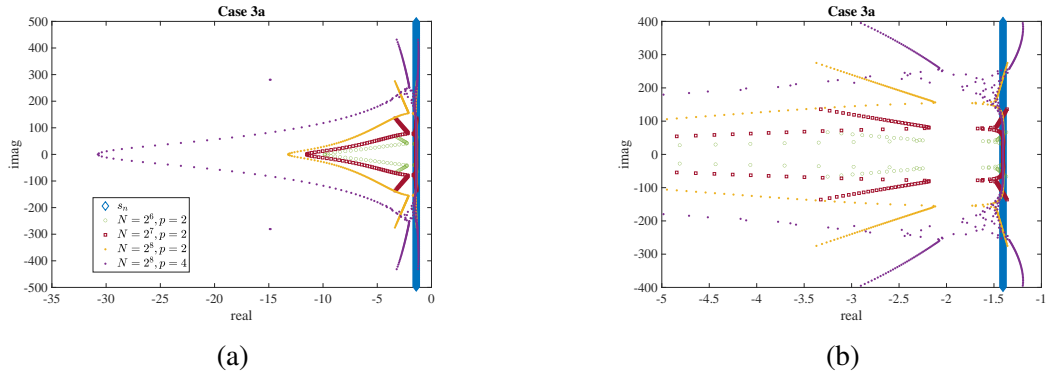


Figure 10: (a) Analytic and numerical spectrum for case 3a, where $a(x) = -0.7 - x, d(x) = -1.3 + 0.1x$ with (b) zoom.

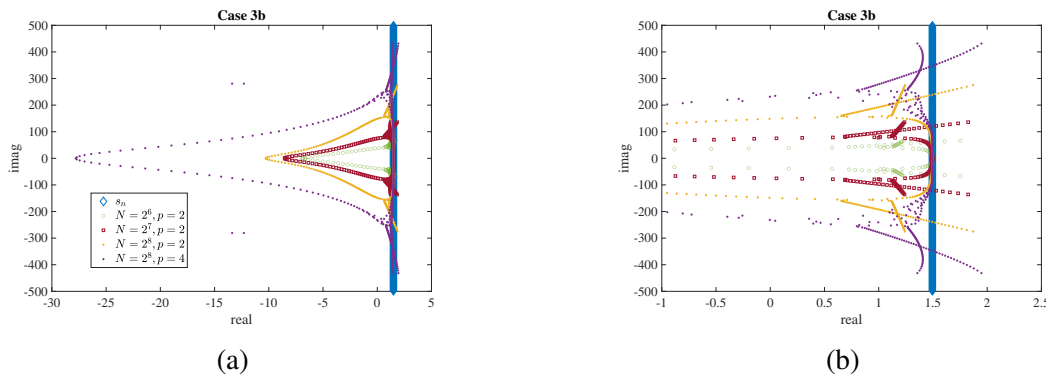


Figure 11: (a) Analytic and numerical spectrum for case 3b, where $a(x) = 0.7 + x, d(x) = 1.3 + 0.1x$ with (b) zoom.

which correspond to physical growth. Figure 6 reflects similar findings to that of Case 1a, with the real part of the discrete spectrum bounded above by $d = 1.3$.

For Case 2a, we have the real root $s_0 = -2$ as well as the complex roots (with non-zero imaginary

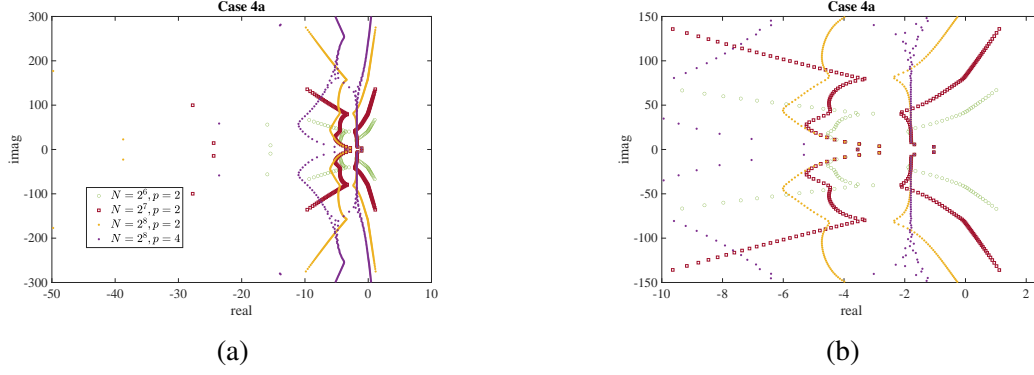


Figure 12: (a) Analytic and numerical spectrum for case 4a, where $a(x) = x, b(x) = -3x, c(x) = 3x, d(x) = -5x$ with (b) zoom.

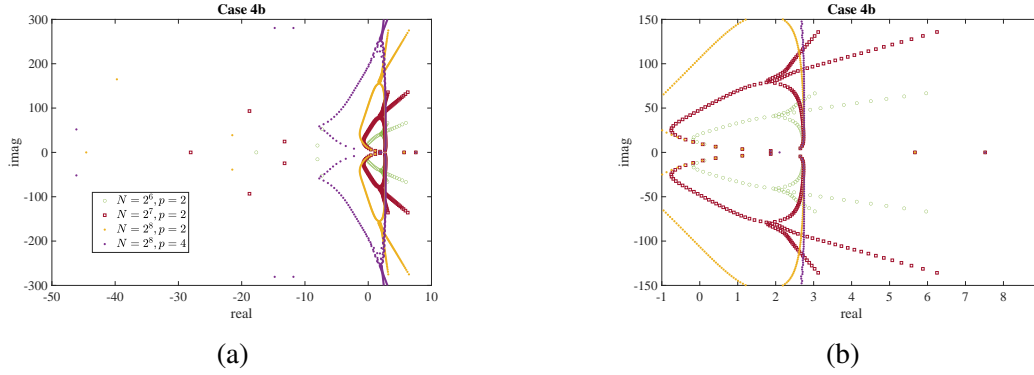


Figure 13: (a) Analytic and numerical spectrum for case 4b, where $a(x) = 2 + x, b(x) = 3x, c(x) = 2x, d(x) = -1 + 4x$ with (b) zoom.

part)

$$s_n^\pm = -2 \pm \sqrt{-9 - 0.36\pi^2 n^2}, \quad n = 1, 2, \dots, \quad (74)$$

with real part $\text{Re}(s_n^\pm) = -2$ corresponding to physical decay. Figure 8 shows that some of the discrete eigenvalues have positive real part that remains bounded above by $a = 1$ (and is therefore not a numerical instability) but tend towards s_n as the mesh is refined or p increases. To the left of s_n , the discrete spectra corresponding to $p = 2$ appears to persist with mesh refinement, which at first led us to believe that physical eigenvalues existed here. However, these do not persist with increasing p , rendering them numerical features.

For case 2b, we have the real root $s_0 = 5$ as well as

$$s_n^\pm = 3 \pm \sqrt{6 - 0.36\pi^2 n^2}, \quad n = 1, 2, \dots$$

which generates real roots $s_1^+ \approx 4.5, s_1^- \approx 1.4$ with the remaining being complex roots with non-zero imaginary part and $\text{Re}(s_n) = 3$, indicating physical growth. All three real eigenvalues are captured by the discretization, as illustrated in Figure 9 and the discretization appears to converge (again from the right, although the real part of the eigenvalues containing non-zero imaginary parts are

bounded above by $d = 4$). It is perhaps not unsurprising that in Cases 1 and 2, the real part of the discrete spectrum (for eigenvalues with non-zero imaginary part) is bounded above by the largest diagonal element of \tilde{B} ; the proof that this is always the case is left for future work.

For Case 3a, all the eigenvalues lay on a vertical line at $\text{Re}(s_n) \approx -1.4$, as evident in Figure 10. The discrete eigenvalues all have negative real part (indicating a stable discretization) and appear to converge to s_n from the right. $a(x) = -0.7 - x$ attains its maximum value of -0.7 on $x \in [0, 2]$ at $x = 0$ and $d(x) = -1.3 + 0.1x$ attains a maximum of -1.1 at $x = 2$, the latter of which appears to provide an upper bound on the real part of the discrete spectrum. The observation that discrete eigenvalues with non-zero imaginary part are bounded above by the maximum value attained on the diagonal of \tilde{B} persists in the remaining cases with variable coefficients. For Case 3b, $\text{Re}(s_n) \approx 1.49$, with some discrete eigenvalues to the right, which appear to have real part bounded above the maximum value that $a(x)$ attains on $x \in [0, 2]$, although the bound is not as tight as in the constant coefficient case, see Figure 11. For Case 4 we do not have an analytic spectrum with which to compare. However, the discrete spectrum shown in Figure 12 suggests negative growth, as eigenvalues that lay to the right of zero do not persist with mesh refinement or increasing order of accuracy. For Case 4b, the spectrum shown in Figure 12 suggests a physical instability is present as discrete eigenvalues with positive real part persist with mesh refinement and increasing p , namely at the complex numbers with $\text{Re}(z) \approx 2, 2.7$ and 7.5 .

7 Conclusions

In this work we derived analytic spectra and solutions to systems of hyperbolic partial differential equations with variable coefficients that arise in perturbed problems, for example when linearizing a nonlinear system around a steady-state solution. We developed a provably stable semi-discretization based on high-order SBP-SAT finite difference schemes in order to explore numerical investigations of physical instabilities. While we did not obtain a strictly stable method of dissipative type (so that the growth rate of the discretization is bounded by that of the continuous) we did observe convergence of the discrete spectrum.

We conclude by stating that caution should be taken when using discrete methods to approximate continuous spectra. A method that is provably stable is desirable, and demonstration of numerical convergence will ensure that positive eigenvalues are physical and not a result of a numerical instability. When the analytic spectra and/or solutions cannot be computed in closed form, discrete approximations to the spectra should exhibit convergence with both mesh-refinement and with higher-order spatial accuracy in order to gain assurance that one is well-capturing the underlying physics.

A

Equation (23) has no spectrum if $R_0 R_L = 0$. To see this, assume WLOG that $R_0 = 0$ and $R = R_L$. Then (23) reduces to

$$\exp[\lambda_1(s)L] (-1 + Rv_1^{(2)})v_2^{(2)} + \exp[\lambda_2(s)L] (1 - Rv_2^{(2)})v_1^{(2)} = 0. \quad (75)$$

If $\exp [\lambda_1(s)L] = \exp [\lambda_2(s)L]$ then (75) further reduces to

$$\exp [\lambda_1(s)L] [(-1 + Rv_1^{(2)})v_2^{(2)} + (1 - Rv_2^{(2)})v_1^{(2)}] = 0, \quad (76)$$

which can only be true if $v_1 = v_2$; which contradicts the linear independence of the eigenvectors. Thus $\exp [\lambda_1(s)L] \neq \exp [\lambda_2(s)L]$, so the only way (23) has roots is where both

$$[-1 + Rv_1^{(2)}]v_2^{(2)} = 0, \quad (77a)$$

$$[1 - Rv_2^{(2)}]v_1^{(2)} = 0. \quad (77b)$$

Attempting to solve (77) requires that $v_1 = v_2$, again a contradiction.

Acknowledgements

B.A.E. was funded by National Science Foundation awards #2036980 and #2053372.

References and Notes

1. M. A. Scheel, T. W. Baumgarte, G. B. Cook, S. L. Shapiro, S. A. Teukolsky, Treating instabilities in a hyperbolic formulation of Einstein's equations, *Phys. Rev. D* 58 (1998) 044020. doi : 10.1103/PhysRevD.58.044020.
2. J. Ferreira, D. Jordão, L. Pinto, Approximating coupled hyperbolic–parabolic systems arising in enhanced drug delivery, *Comput. Math. Appl.* 76 (1) (2018) 81–97.
3. L. Karlstrom, E. Dunham, Excitation and resonance of acoustic-gravity waves in a column of stratified, bubbly magma, *J. Fluid Mech.* 797 (2016) 431–470.
4. K. L. Zapadka, F. J. Becher, A. L. Gomes dos Santos, S. E. Jackson, Factors affecting the physical stability (aggregation) of peptide therapeutics, *Interface Focus* 7 (6) (2017) 20170030.
5. M. A. Blanco, Computational models for studying physical instabilities in high concentration biotherapeutic formulations, *mAbs* 14 (1) (2022) 2044744. doi : 10.1080/19420862.2022.2044744.
6. A. J. Hale, Magma flow instabilities in a volcanic conduit: Implications for long-period seismicity, *Phys. Earth and Planet. Inter.* 163 (1) (2007) 163–178.
7. V. M. Yarushina, D. Bercovici, C. Michaut, Two-phase dynamics of volcanic eruptions: Particle size distribution and the conditions for choking, *J. Geophys. Res.: Solid Earth* 120 (3) (2015) 1503–1522.
8. H. O. Kreiss, G. Scherer, Finite element and finite difference methods for hyperbolic partial differential equations, in: *Mathematical Aspects of Finite Elements in Partial Differential Equations*, Academic Press, 1974, pp. 195–212.

9. H. O. Kreiss, G. Scherer, On the existence of energy estimates for difference approximations for hyperbolic systems, in: Technical report, Uppsala University Dept of Scientific Computing Uppsala, Sweden, 1977.
10. B. Strand, Summation by parts for finite difference approximations for d/dx , *J. Comput. Phys.* 110 (1) (1994) 47–67.
11. D. C. D. R. Fernández, J. E. Hicken, D. W. Zingg, Review of summation-by-parts operators with simultaneous approximation terms for the numerical solution of partial differential equations, *Comput. Fluids* 95 (2014) 171 – 196.
12. M. Svärd, J. Nordström, Review of summation-by-parts schemes for initial-boundary-value problems, *J. Comput. Phys.* 268 (2014) 17 – 38.
13. H. Ranocha, Generalised summation-by-parts operators and variable coefficients, *J. Comput. Phys.* 362 (2018) 20 – 48. doi:<https://doi.org/10.1016/j.jcp.2018.02.021>.
14. B. Gustafsson, H.-O. Kreiss, J. Oliger, *Time-Dependent Problems and Difference Methods*, Wiley, 2013.
15. J. Awrejcewicz, *Dynamical Systems: Theoretical and Experimental Analysis*: Łódź, Poland, December 7-10, 2015, *Springer Proceedings in Mathematics & Statistics*, Springer International Publishing, 2016.
16. M. H. Carpenter, D. Gottlieb, S. Abarbanel, Time-stable boundary conditions for finite-difference schemes solving hyperbolic systems: Methodology and application to high-order compact schemes, *J. Comput. Phys.* 111 (2) (1994) 220 – 236.
17. J. Nordström, A. A. Ruggiu, On conservation and stability properties for summation-by-parts schemes, *J. Comput. Phys.* 344 (2017) 451 – 464.
18. T. C. Fisher, M. H. Carpenter, J. Nordström, N. K. Yamaleev, C. Swanson, Discretely conservative finite-difference formulations for nonlinear conservation laws in split form: Theory and boundary conditions, *J. Comput. Phys.* 234 (2013) 353 – 375.
19. B. A. Erickson, O. O’Reilly, J. Nordström, Accuracy of stable, high-order finite difference methods for hyperbolic systems with non-smooth wave speeds, *J. Sc. Comput.* 81 (3) (2019) 2356–2387.
20. P. J. Roache, *Verification and validation in computational science and engineering*, Hermosa Publishers, Albuquerque, NM, 1998.
21. J. Nordström, Conservative finite difference formulations, variable coefficients, energy estimates and artificial dissipation, *J. Sci. Comput.* 29 (3) (2006) 375–404.